Spatiotemporal Analysis of Tropospheric Variability Using GNSS Radio Occultation: A Decadal Study

Nithish Manikkavasagam[1], Balaji Devaraju[2]

[1]nmanikkavasa2023@fau.edu,
[2]dbalaji@iitk.ac.in
[1] Department of Civil, Environmental and Geomatics Engineering, Florida Atlantic University, 777 Glades Road, FL 33431, USA
[2] Department of Civil Engineering, Indian Institute of Technology Kanpur, UP 208016, India

KEY WORDS: GNSS-RO; Troposphere, Spatiotemporal Analysis, Climate Records, Atmospheric Profiling.

ABSTRACT:

Global Navigation Satellite System Radio Occultation (GNSS-RO) offers a unique means of retrieving vertical atmospheric profiles with high precision and global coverage. This study investigates the spatiotemporal characteristics of tropospheric parameters temperature, pressure, and humidity using ten years (2007–2016) of Level-3 gridded data from the ROM SAF Climate Data Records. The dataset, processed in NetCDF format, was analyzed using multidimensional array tools to extract monthly, seasonal, and anomaly-based trends within the 0–10 km (troposphere) altitude range and between 40°S and 40°N. Seasonal variations reveal clear hemispheric patterns, with equatorial regions maintaining consistently high values across all parameters. Anomalies indicate that 2016 experienced pronounced warming and increased humidity, while 2008 marked the coldest and driest year in the period studied. Climatological plots confirm a strong dependence of all three parameters on both latitude and altitude, with consistent inversion patterns between hemispheres. By integrating satellite-based atmospheric profiling with spatial and temporal data analysis, this work provides valuable insight into lower atmosphere dynamics and contributes to long-term climate monitoring efforts.

1. INTRODUCTION

Occultation refers to the physical disappearance of an object in the background caused by an intervening object in the foreground, typically the apparently larger one, during their relative motion. In atmospheric science, radio occultation describes the occultation of radio-signal transmitters by astronomical bodies with atmospheres, where the received signal is affected by refractive bending. Atmospheric radio occultation relies on detecting changes in a radio signal as it passes through a planet's atmosphere and becomes partially obscured by it. When electromagnetic radiation propagates through the atmosphere, it undergoes refraction, and the magnitude of this bending depends on the gradient of refractivity along the signal path, which is determined by the atmospheric density gradient (Yu et al., 2014). This effect is especially significant when the signal travels along a long atmospheric limb path.

At radio frequencies, the bending of the signal cannot be measured directly; instead, it is inferred from the observed Doppler shift, given the known geometry of the transmitter and receiver. The derived bending angles can then be related to the refractive index of the atmosphere by applying an Abel transformation to the equation connecting bending angle and refractivity. In the neutral atmosphere (troposphere), this refractivity information enables retrieval of atmospheric temperature, pressure, and water vapor content, making radio occultation a valuable tool for meteorology (Kursinski et al., 2000).

Global Navigation Satellite Systems (GNSS) consist of constellations of Earth-orbiting satellites that broadcast signals describing their precise positions in space and time, along with ground control stations and receiver networks that compute positions using trilateration. GNSS support a wide range of applications across transportation sectors including aviation, maritime, rail, and road—as well as telecommunications, land surveying, emergency response, precision agriculture, mining, and scientific research. These systems underpin critical positioning, navigation, and timing (PNT) infrastructure used to manage air traffic, synchronize computer networks, operate power grids, and more.

Currently, four fully operational global navigation satellite systems GPS (United States), GLONASS (Russia), Galileo (European Union), and BeiDou (China) form the core of the GNSS infrastructure. In addition, regional systems such as IRNSS/NavIC (India) and QZSS (Japan) provide supplementary coverage and enhance positioning accuracy. Historically, only GPS has been used for atmospheric radio occultation, with satellites transmitting primarily at L1 (1.57542 GHz) and L2 (1.2276 GHz). As GPS signals pass through the atmospheric limb, their velocity is modified by the refractive effects of both the ionosphere and the neutral atmosphere, and the signal path becomes bent due to refractive-index gradients.

GNSS radio occultation (GNSS-RO) formerly referred to as GPS-RO extends this concept to signals from all GNSS constellations. First demonstrated in 1995, GNSS-RO is a relatively recent technique for atmospheric profiling and has since become widely used in weather forecasting and climate monitoring. The method involves a low-Earth-orbit (LEO) satellite receiving signals emitted by GNSS satellites. As the signal traverses the atmosphere, it experiences refraction whose magnitude depends on atmospheric temperature and water vapor concentration. Because the relative position of the transmitting GNSS satellite and the receiving LEO satellite changes continuously, GNSS-RO provides a vertical scan of successive atmospheric layers, offering an almost instantaneous depiction of the atmospheric state (Bai et al., 2020). The basic geometry of the GNSS radio occultation technique, including signal bending through the ionosphere and neutral atmosphere, is illustrated in Fig. 1. GNSS-RO observations can also be performed from aircraft or high-elevation ground stations, expanding measurement capability beyond satellite-to-satellite geometries.

2. DATA

The Radio Occultation Meteorology Satellite Application Facility (ROM SAF) is a decentralized processing center under the European Organization for the Exploitation of Meteorological

Satellites (EUMETSAT). ROM SAF is responsible for the operational processing of GNSS Receiver for Atmospheric Sounding (GRAS) radio occultation (RO) data from the Metop and Metop-SG satellites, as well as RO data from multiple international missions (ROM SAF, 2022). It provides bending angle, refractivity, temperature, pressure, humidity, and other geophysical variables in near–real time for numerical weather prediction (NWP), along with reprocessed Climate Data Records (CDRs) and Interim Climate Data Records (ICDRs), which offer improved temporal consistency for climate applications. ROM SAF also produces globally gridded monthly-mean RO climatology used extensively for climate monitoring. In addition, ROM SAF maintains the Radio Occultation Processing Package (ROPP), a software suite that supports users in processing, quality-controlling, and assimilating RO data from any mission into NWP models and other atmospheric applications. RO data from Metop/Metop-SG and other missions are distributed according to data levels (0–3) and product types (NRT, Offline, CDR, and ICDR). These categories are summarized below.

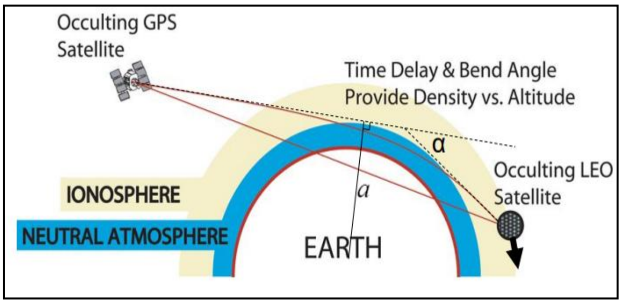

Figure 1. Schematic representation of the GNSS radio occultation (GNSS-RO) measurement geometry.

2.1 Data Levels

- **Level 0**: Raw sounding, tracking, and ancillary GNSS data prior to clock correction and reconstruction.
- **Level 1A**: Reconstructed full-resolution excess phases, total phases, pseudo ranges, SNR, orbital information, I/Q values, NCO carrier phases, navigation bits, and quality flags.
- **Level 1B**: Bending angles and impact parameters, tangent-point locations, and associated quality information.
- **Level 2**:
    - **Level 2A**: Refractivity, geopotential height, and dry-temperature profiles.
    - **Level 2B**: Pressure, temperature, and specific humidity profiles.
    - **Level 2C**: Surface pressure, tropopause height, and planetary boundary-layer height.
    - **Level 2D**: ECMWF model-level coefficients.
- **Level 3**: Gridded or resampled RO products derived from Level 1 or Level 2 data, including daily, monthly, or seasonal averages on a global spatiotemporal grid, along with metadata, uncertainty estimates, and quality information.

2.2 Product Types

- **NRT (Near Real-Time):** Delivered within
    - < 3 hours (ROM SAF Level 2 for EPS),
    - < 150 minutes (EPS-SG Global Mission),
    - < 125 minutes (EPS-SG Regional Mission).
- **Offline Products:** Delivered from 5 days up to 6 months after measurement. These incorporate scientific upgrades and improved algorithms.
- **CDR (Climate Data Record):** Produced from dedicated reprocessing using a fixed processing chain, covering multi-year time periods and ensuring high homogeneity for climate studies.
- **ICDR (Interim Climate Data Record):** Extends a CDR forward in time using a system consistent with the original CDR but delivered with lower latency, ensuring continuity for climate applications.

A summary of the datasets used in this study is provided in Table 1.

Data Source	METOP
Data Level	Level 3(grid data)
Parameter Analyzed	Temperature, Pressure and Humidity
Time period of Analysis	2007-2016
Data Access	ROMSAF-CDR
Data Format	NetCDF4
Dimensions of Data	(LATITUDE x LONGITUDE x ALTITUDE x TIME)

Table 1: Summary of the Data Used in This Study

3. METHODS

For this study, the workflow followed from data access to visualization and analysis is summarized in Fig. 2

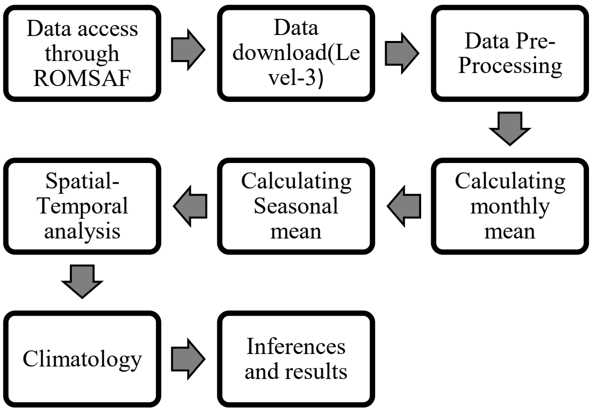

Figure 2. The complete processing workflow used in this study.

3.1 Data Access and Download

The required GNSS-RO data were accessed through the ROM SAF product archive. After registering on the ROM SAF portal, Level-3 gridded Climate Data Record (CDR) datasets were downloaded for Metop satellites for the period 2007–2016. The downloaded files are of type zgrid and provided in NetCDF-4 format, with a monthly temporal resolution.

Coordinates and dimensions of the dataset:

- **Latitude:** 87.5° S to 87.5° N at 5° intervals
- **Altitude:** 0–50 km at 200 m vertical resolution
- **Longitude:** Zonal mean values (180°)
- **Time:** Monthly data from December 2006 to December 2016.

3.2 Data Pre-processing and Mean Estimation

The data were processed using Xarray, a Python library designed for efficient handling of large multidimensional datasets (Hoyer, and Hamman, 2017). Initial cleaning was performed to remove missing and null values.

Monthly means were computed using:

$$Monthly\ mean = f(x) = \sum_{i=1}^{10} \frac{x_i}{10} \tag{1}$$

Here, the index i=1…10corresponds to the ten-year analysis period (2007–2016).

The resulting monthly mean values were then used to compute seasonal means as per table 2.

December	January	February	**Winter**	
March	April	May	**Spring**	**Pre - Monsoon**
June	July	August	**Summer**	**Monsoon**
September	October	November	**Fall**	**Post Monsoon**

Table 2: Definition of Seasons and Monsoons

Variations of temperature, pressure, and humidity were analyzed for each month and season as a function of latitude. Since the troposphere extends approximately up to 10 km, the dataset was vertically truncated to 0–10 km for focused analysis.

Although seasonal analysis provides insight, it does not represent time continuously. Therefore, to better capture temporal evolution, a spatiotemporal analysis was performed where time (months) forms one axis and latitude forms the other.

3.3 Spatiotemporal Analysis

Spatiotemporal analysis involves studying variations across both space and time. In this work, anomalies were calculated for each parameter to characterize temporal variability in the troposphere.

The anomaly for a given value x is computed as:

$$f(x) = x - \bar{x} \tag{2}$$

Anomalies were computed for every month from 2007 to 2016 and extracted for the tropospheric layer (0–10 km). For more detailed interpretation, this range was divided into three sub-layers: (i) 0-2 km; (ii) 2 – 5 km; (iii) 5 – 10 km. Latitude was restricted to 40° S to 40° N, where tropospheric processes are most prominent. For each classification of altitude, anomaly matrices were generated with time as the index and latitude as columns. A colormesh plot was then produced for each parameter (temperature, pressure, humidity), clearly showing their spatiotemporal evolution over the study period.

3.4 Climatology

Climatology represents the average behavior of an atmospheric parameter as a function of month and latitude. It was computed using:

$$climatology = f(month, latitude) \tag{11}$$

Climatology plots were generated for each of the three altitude categories (0–2 km, 2–5 km, 5–10 km), providing a comprehensive view of long-term seasonal patterns across the troposphere.

4. RESULTS

The characteristics of the troposphere were analyzed using GPS-RO data under three stages:

i. Seasonal / Monsoon-based analysis
ii. Anomaly-based analysis
iii. Climatology-based analysis

i) Based on Season / Monsoon

a) Temperature

Temperature trends were analyzed with respect to latitude (Figure 3). Temperature decreases with altitude, and the equatorial region (0° latitude) consistently exhibits the highest temperature.

Winter (December–February):

In December, temperatures gradually increase from 90°S, peak at the equator, and decrease toward 90°N. In January, temperatures in the Southern Hemisphere (especially after 60°S) slightly decline compared to December, while the Northern Hemisphere warms slightly. February shows a further temperature decrease from 30°N.

Spring / Pre-Monsoon (March–May):

March follows a pattern similar to winter. In April, the pattern reverses—temperature decreases more rapidly toward the Southern Hemisphere than the Northern Hemisphere, and variations between 25°S and 25°N are minimal. In May, the hemispheric contrast increases, with rising temperatures from 30°N compared to April.

Summer / Monsoon (June–August):

This season exhibits the strongest temperature contrast between hemispheres. June follows the May pattern in the Southern Hemisphere, but in the Northern Hemisphere (particularly north of 25°N), temperature drop becomes less significant. July and August follow similar distributions.

Fall / Post-Monsoon (September–November):

This season shows a pattern similar to summer, though with reduced contrast between hemispheres. In September, temperatures are lowest near 90°S, rise toward the equator, and then slowly decrease. In October and November, temperatures start decreasing from 30°N.

b) Pressure

Pressure trends were analyzed with respect to latitude (Figure 4).

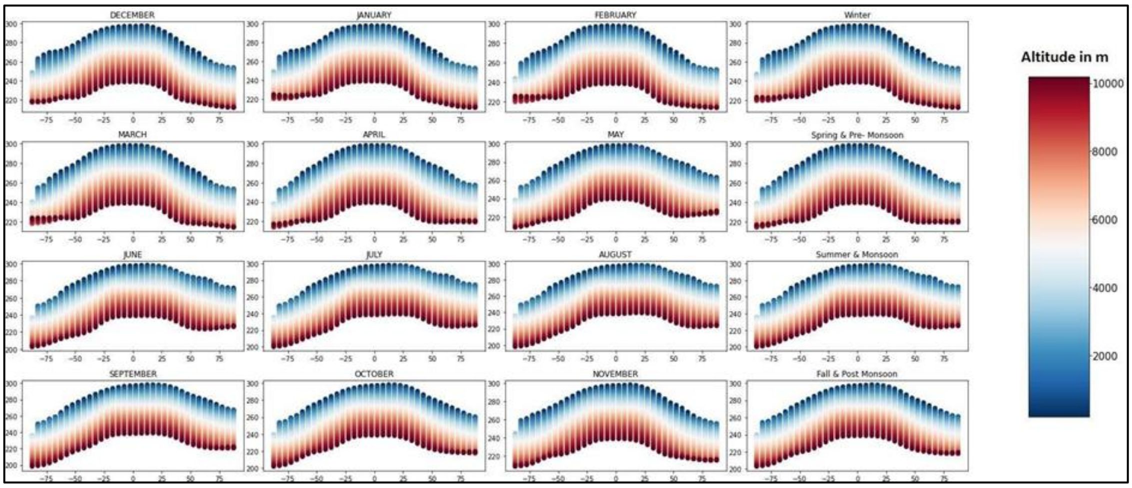

Figure 3. Latitude vs. Temperature

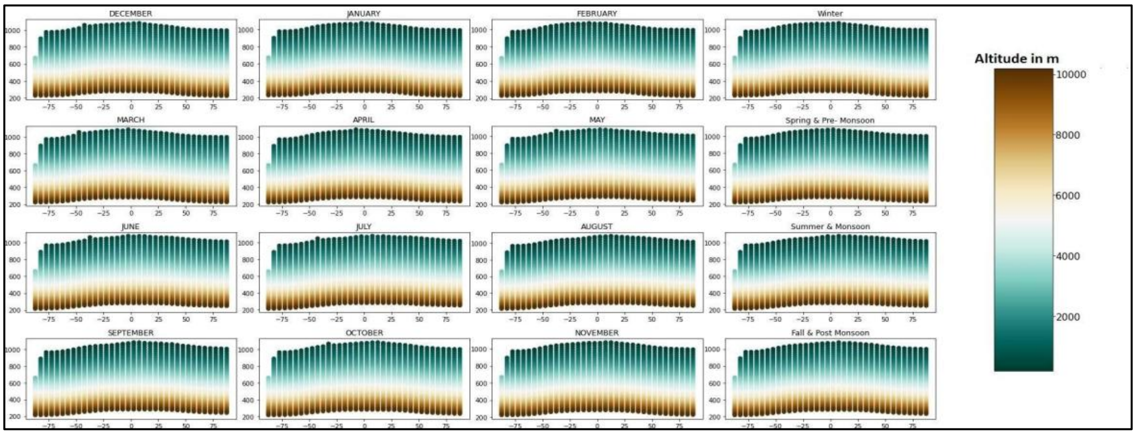

Figure 4. Latitude vs. Pressure

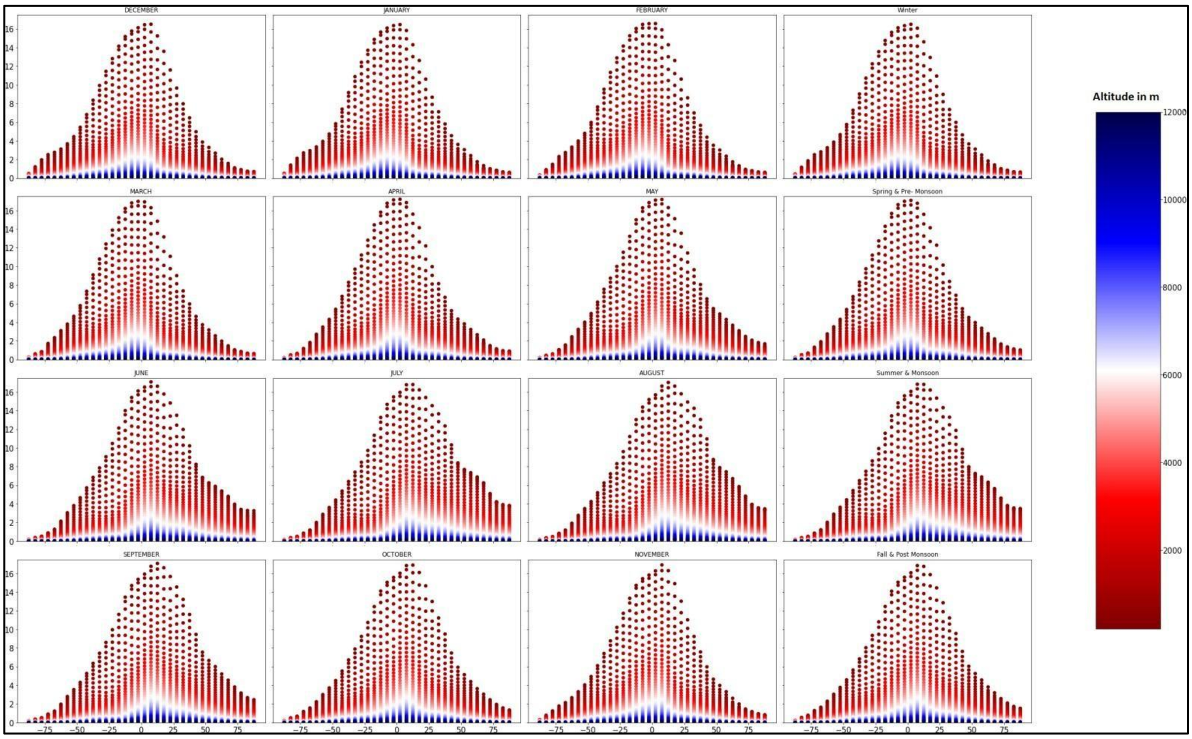

Figure 5. Latitude vs Humidity

Pressure decreases with altitude, and the equatorial band (10°S–10°N) has the highest pressure.

Winter (December–February):

Pressure follows a smooth bell-shaped curve: low at 90°S, gradually rising to a peak at the equator, and decreasing symmetrically toward 90°N. Pressure differences between hemispheres are minimal.

Spring / Pre-Monsoon (March–May):

March resembles winter. In April and May, the pressure difference between hemispheres increases. Beyond 50°N, pressure decreases more gradually compared to winter, resulting in overall higher values at these latitudes.

Summer / Monsoon (June–August):

From 25°N upward, the pressure drop is smaller compared to May, producing the highest recorded pressure differences between hemispheres. Pressure north of 25°N is higher than in winter and spring.

Fall / Post-Monsoon (September–November):

September resembles summer. In October, pressure begins decreasing, and by November the trend becomes similar to December. Overall, fall conditions lie between summer and spring, especially beyond 50°N.

c) Humidity

Humidity also decreases with altitude (Figure 5). The equatorial region (25°S–25°N) shows the highest values.

Winter (December–February):

Humidity near 75°S is ~0.8 g/kg and rises toward the equator. The Southern Hemisphere shows higher humidity than the Northern Hemisphere. In December, the peak is slightly north of the equator; in January and February it shifts closer to 0°.

Spring / Pre-Monsoon (March–May):

March resembles winter. In April, humidity begins increasing in the Northern Hemisphere, particularly after 50°N. By May, the humidity peak shifts northwards.

Summer / Monsoon (June–August):

From June to August, the humidity peak gradually shifts further into the Northern Hemisphere (10–12°N). Humidity increases significantly from 30°N.

Fall / Post-Monsoon (September–November):

September resembles August. In October and November, humidity decreases north of 30°N, and the peak shifts toward the equator, though not fully aligned with it.

ii) Based on Anomalies

a) Temperature Anomalies

Figure 6 clearly shows that 2016 is the warmest year, while 2008 is the coldest. A notable temperature rise occurs in 2010. Between 2011 and 2016, temperature anomalies transition progressively from cold to warm. There is no consistent latitudinal pattern. Temperature anomalies increase with altitude,

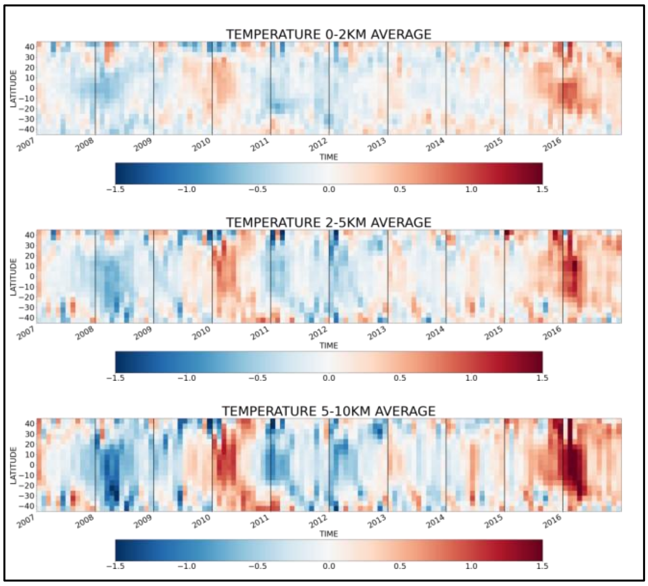

Figure. 6 Temperature Anomalies

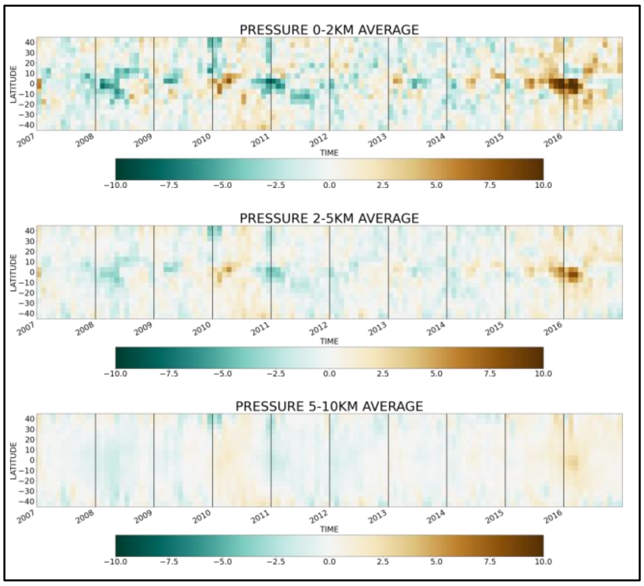

Figure. 7 Pressure Anomalies

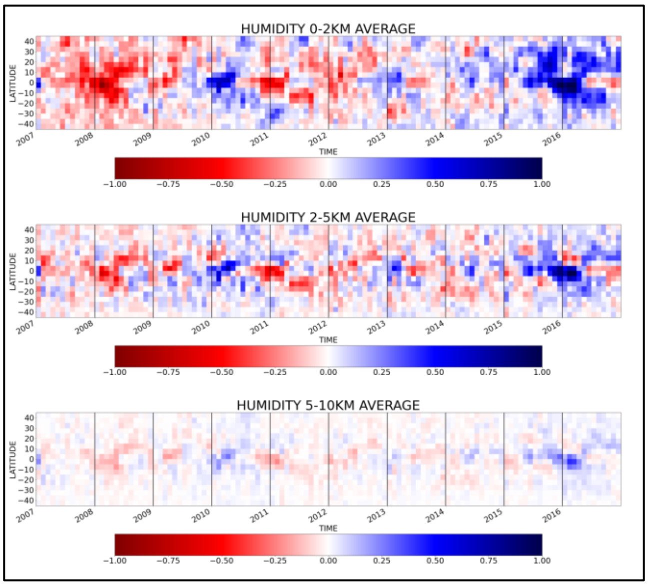

Figure. 8 Humidity Anomalies

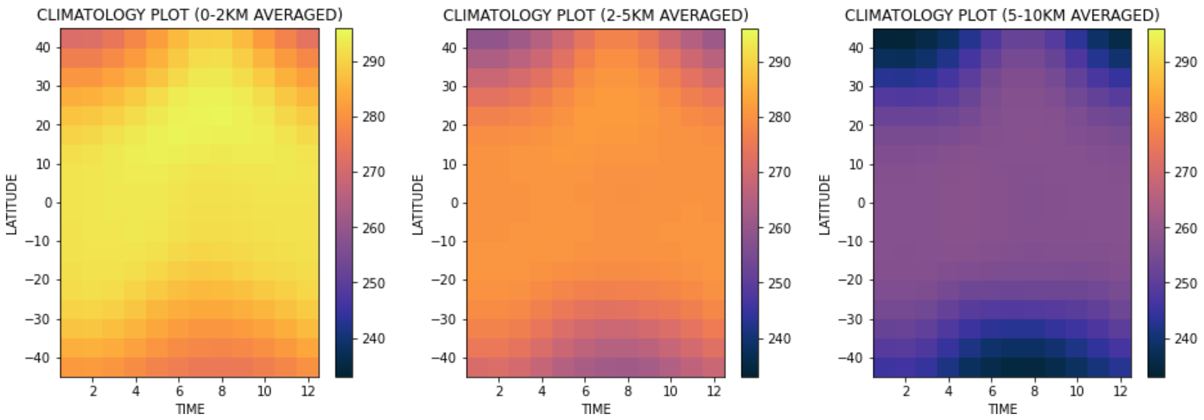

Figure 9: Climatology of Temperature

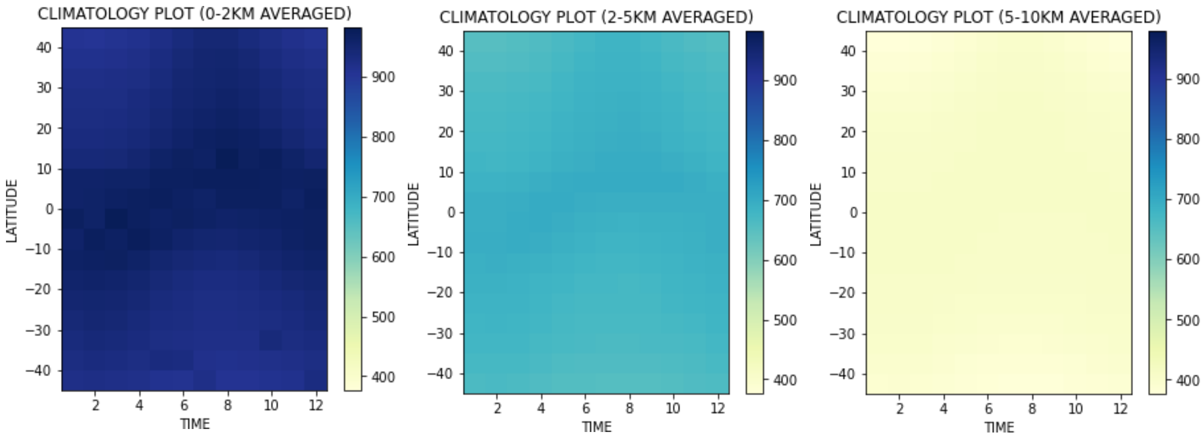

Figure 10: Climatology of Pressure

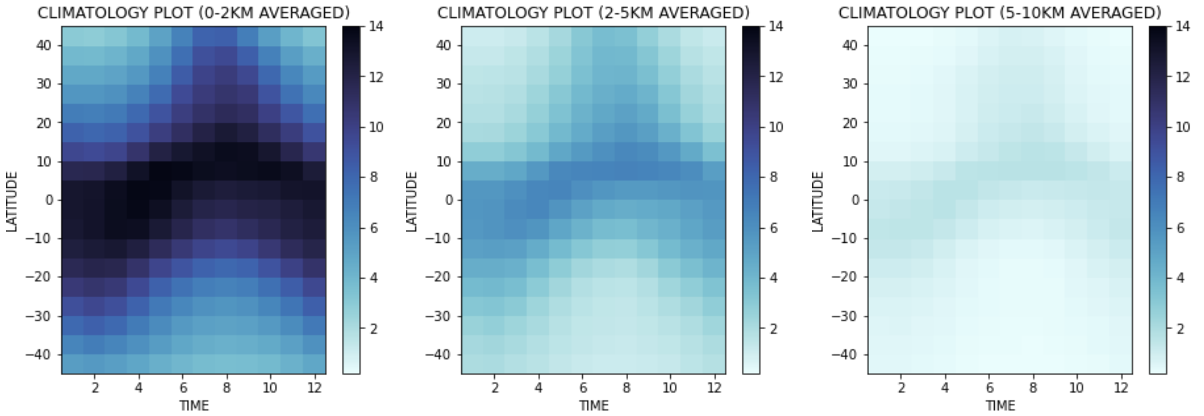

Figure 11: Climatology of Humidity

as shown across the three altitude bands.

b) Pressure Anomalies

Figure 7 reveals pressure anomalies are most prominent in the equatorial region (10°S–10°N). Late 2015 and early 2016 show above-normal pressure. No regular temporal or latitudinal patterns are observed. Below-normal pressure is recorded in 2008, late 2010, and early 2011. Pressure anomalies decrease with altitude.

c) Humidity Anomalies

Figure 8 reveals humidity anomalies show highest positive values in 2016 and lowest in 2008. Early 2010 also shows elevated humidity but not as strong as 2016. No clear temporal or latitudinal pattern is observed. Humidity anomalies decrease with altitude, as indicated across the panels.

iii) Climatology

a) Temperature Climatology

As per figure 9, temperature remains consistently high between 15°S and 15°N throughout the year. In the Northern Hemisphere, temperatures are lowest in January, peak in July–August, and then decline. The Southern Hemisphere shows the opposite trend. Temperature decreases with increasing distance from the equator and with altitude, as seen when comparing the 0–2 km, 2–5 km, and 5–10 km plots.

b) Pressure Climatology

As per figure 10, pressure strongly decreases with altitude—highest in 0–2 km and lowest in 5–10 km. Maximum pressure occurs between 10°S and 10°N. In the Northern Hemisphere, pressure is lowest in January and highest around July–August; the Southern Hemisphere displays the opposite seasonal cycle. Pressure exhibits stronger seasonal variation compared to temperature and humidity.

c) Humidity Climatology

As per figure 11, humidity decreases significantly with altitude and is highest in the equatorial region. Latitudinal and seasonal behavior follow the same broad pattern as temperature and pressure.

5. CONCLUSION

The spatio-temporal characteristics of the troposphere were analyzed using GPS-RO observations. The analysis shows that 2016 exhibited above-normal values for all parameters, whereas 2008 showed the opposite condition. With increasing altitude, anomalies of pressure and humidity decrease, while temperature anomalies increase. Overall, temperature, pressure, and humidity decrease with increasing distance from the equator, and all three parameters are inversely related to altitude above mean sea level.

In the Northern Hemisphere, for each latitude, these parameters are lowest in January, gradually increase, reach their maximum during July and August, and then decrease toward December. The Southern Hemisphere shows the reverse pattern. During winter, the differences in temperature, pressure, and humidity between the hemispheres are minimal. As time progresses into spring/pre-monsoon, these hemispheric differences increase. From about 30°N, during spring/pre-monsoon, the rate of decrease in temperature, pressure, and humidity becomes smaller, resulting in higher parameter values. Summer/monsoon exhibits the maximum hemispheric contrast, while fall/post-monsoon shows differences that lie between those of summer and spring.

REFERENCES

Bai, W., Deng, N., Sun, Y., Du, Q., Xia, J., Wang, X., ... & Liu, X. (2020). Applications of GNSS-RO to numerical weather prediction and tropical cyclone forecast. Atmosphere, 11(11), 1204.

Hoyer, S., & Hamman, J. (2017). xarray: ND labeled arrays and datasets in Python. Journal of Open Research Software, 5(1), 10–10.

Kursinski, E. R., Hajj, G. A., Leroy, S. S., & Herman, B. (2000). The GPS radio occultation technique. Terrestrial Atmospheric and Oceanic Sciences, 11(1), 53–114.

ROM SAF. (2022). Product user manual: Level 3 gridded products (Version 3.0). EUMETSAT. https://www.romsaf.org

Yu, K., Rizos, C., Burrage, D., Dempster, A. G., Zhang, K., & Markgraf, M. (2014). An overview of GNSS remote sensing. EURASIP Journal on Advances in Signal Processing, 2014(1), 134.